Surface Emissivity at Microwaves to Millimeter Waves over Polar Regions: Parameterization and Evaluation with Aircraft Experiments

D. Wang, C. Prigent, L. Kilic, S. Fox, C. Harlow, C. Jimenez, F. Aires, C. Grassotti, F. Karbou

Surface Emissivity at Microwaves to Millimeter Waves over Polar Regions: Parameterization and Evaluation with Aircraft Experiments

D. WANG,[a] C. PRIGENT,[b] L. KILIC,[a] S. FOX,[c] C. HARLOW,[c] C. JIMENEZ,[d] F. AIRES,[b] C. GRASSOTTI,[e,f,g] AND F. KARBOU[h]

[a] *LERMA, Observatoire de Paris, Paris, France*
[b] *LERMA, CNRS, Observatoire de Paris, Paris, France*
[c] *Met Office, Exeter, United Kingdom*
[d] *LERMA, Estellus, Paris, France*
[e] *Earth System Science Interdisciplinary Center, University of Maryland, College Park, College Park, Maryland*
[f] *Cooperative Institute for Climate and Satellites—Maryland, University of Maryland, College Park, College Park, Maryland*
[g] *NOAA/NESDIS/STAR, University of Maryland, College Park, College Park, Maryland*
[h] *CNRM-GAME, Météo-France, CNRS, Saint Martin d'Hères, France*

(Manuscript received 1 October 2016, in final form 15 December 2016)

ABSTRACT

The Tool to Estimate Land Surface Emissivity from Microwave to Submillimeter Waves (TELSEM^2) is linked to a climatology of monthly emissivity estimates and provides a parameterization of the surface emissivity up to 700 GHz, in the framework of the preparation for the Ice Cloud Imager (ICI) on board the Meteorological Operational Satellite Second Generation (MetOp-SG). It is an updated version of the Tool to Estimate Land Surface Emissivities at Microwave Frequencies (TELSEM; Aires et al. 2011). This study presents the parameterization of continental snow and ice and sea ice emissivities in TELSEM^2. It relies upon satellite-derived emissivities up to 200 GHz, and it is anchored to the Special Sensor Microwave Imager (SSM/I) TELSEM monthly climatology dataset (19–85 GHz). Emissivities from Météo-France and the National Oceanic and Atmospheric Administration (NOAA) at frequencies up to 190 GHz were used, calculated from the Special Sensor Microwave Imager/Sounder (SSMIS) and the Advanced Microwave Sounding Unit-B (AMSU-B) observations. TELSEM^2 has been evaluated up to 325 GHz with the observations of the International Submillimeter Airborne Radiometer (ISMAR) and the Microwave Airborne Radiometer Scanning System (MARSS), which were operated on board the Facility for Airborne Atmospheric Measurements (FAAM) aircraft during the Cold-Air Outbreak and Submillimeter Ice Cloud Study (COSMICS) campaign over Greenland. Above continental snow and ice, TELSEM^2 is very consistent with the aircraft estimates in spatially homogeneous regions, especially at 89 and 157 GHz. Over sea ice, the aircraft estimates are very variable spatially and temporally, and the comparisons with the TELSEM^2 were not conclusive. TELSEM^2 will be distributed in the new version of the RTTOV radiative transfer community code, to be available in 2017.

1. Introduction

The current passive microwave instruments on board meteorological satellites are limited in frequencies to 200 GHz. The Ice Cloud Imager (ICI), on board the next generation of European operational meteorological satellites [EUMETSAT Polar System Second Generation (EPS-SG)], will observe the frequencies up to 664 GHz. It will expand the current capabilities for the characterization of the cloud frozen phase, but this is challenging, as the radiative transfer models have not been fully developed and evaluated yet up to these frequencies. More specifically, no effort has been made yet toward the estimation of the surface emissivity at frequencies above 200 GHz.

Under a large range of atmospheric conditions, satellite observations above 200 GHz will not be sensitive to the surface contribution, due to the increased atmospheric opacity with frequency. However, for dry atmospheres, a portion of the signal received by the satellite can come from the surface [see Fig. 1, which presents the total atmospheric transmission at nadir, as calculated by the Atmospheric Radiative Transfer Simulator (ARTS; Eriksson et al. 2011), for

Corresponding author e-mail: D. Wang, die.wang@obspm.fr

DOI: 10.1175/JTECH-D-16-0188.1

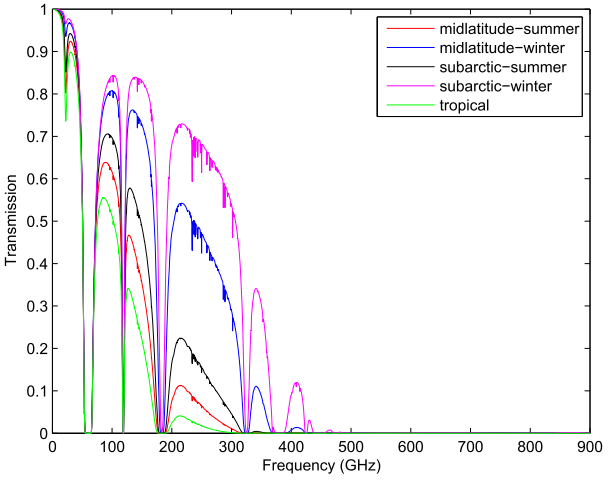

FIG. 1. Total transmission of the atmosphere at nadir, as calculated with ARTS, for five standard atmospheres from FASCOD.

five standard atmospheres from the Fast Atmospheric Signature Code (FASCOD)]. Under dry and cold conditions, a reliable estimate of the surface emissivity is necessary to account for the surface contribution and to perform an accurate retrieval of the atmospheric properties. Atmospheric transmission at high frequencies occurs primarily around the poles and at midlatitudes during winter, even up to 480 GHz (Fig. 1).

Physical modeling (e.g., numerical modeling, theoretical modeling) of the emissivity of snow and ice at microwave frequencies is particularly complex, given the large variety of snow and ice signatures in this frequency range. The interaction between the radiation and snow/ice involves both volume and surface scattering, and the mechanisms are very variable in space and time. A variety of models exists (see Mätzler 2006 for a review). Four major models are available to the community: the Community Radiative Transfer Model (CRTM) from NOAA (Weng et al. 2001), the single-layer model from the Helsinki University of Technology (HUT) (Pulliainen et al. 1999), the Microwave Emission Model of Layered Snowpack (MEMLS) from the University of Bern [Wiesmann and Mätzler (1999), adapted by Tonboe (2010) for sea ice], and the Dense Media Radiative Transfer (DMRT) snow models (Tsang et al. 2007; Picard et al. 2013). However, the need for a detailed description of the snow and ice parameters (e.g., the snow grain size distribution, the stratification of the snow medium, and the quantification of the brine inclusion in sea ice) makes it very difficult to provide realistic estimates at continental scales, where such information is clearly not available. Even if a perfect model existed, the lack of reliable input parameters would jeopardize its robustness. Modeling results above 100 GHz can be very misleading, as the complexity of the interaction of the radiation and the surface might not be taken into account at high frequencies. Some efforts to validate MEMLS have been conducted, with airborne measurements between 89 and 190 GHz (Harlow 2011; Harlow and Essery 2012). However, even under controlled environments, the modeling of emissivity above 100 GHz is very challenging.

Microwave emissivities have also been calculated directly from satellite observations, removing the atmospheric contribution (gas and clouds) and the modulation by the land surface temperature. This technique has been applied to conical imagers such as the SSM/I, the Tropical Rainfall Measuring Mission (TRMM) Microwave Imager (TMI), and the Advanced Microwave Scanning Radiometer for Earth Observing System (AMSR-E) (e.g., Prigent et al. 1997, 2005, 2006; Moncet et al. 2011) but also to cross-track sounders such as AMSU (e.g., Prigent et al. 2005; Karbou et al. 2005; Karbou and Prigent 2005). These estimates capture well the spatial and temporal variabilities of the emissivities. An analysis of the spectral, angular, and polarization dependences of these satellite-derived emissivities was conducted (Prigent et al. 2008), and led to the development of the Tool to Estimate Land Surface Emissivities at Microwave Frequencies (TELSEM). TELSEM provides a parameterization of the emissivity for all observing conditions and for all continental surfaces, given the surface location and month in the year, for frequencies from 19 to 90 GHz. It is anchored to a robust climatology of 19–85 GHz emissivities, calculated from 15 years of SSM/I observations (Prigent et al. 2006). Compared to model calculations (e.g., CRTM), TELSEM provides emissivity estimates that agree better with satellite observations up to 90 GHz, especially over polar regions (Bernardo et al. 2013; Prigent et al. 2015).

Most satellite-derived emissivity studies so far have focused on the frequency range up to 100 GHz, where the atmospheric transmission is significant. Between 100 and 200 GHz, the need for reasonable estimates of the emissivity at the AMSU, Microwave Humidity Sounder (MHS), SSMIS, and Advanced Technology Microwave Sounder (ATMS) window channels around 160 GHz has triggered some efforts (e.g., at Météo-France; Karbou et al. 2014), at NOAA, and at the Met Office), but they have not been consolidated yet. The snow and ice emissivities have been estimated from aircraft observations at AMSU frequencies up to 190 GHz, on board the U.K. Facility for Airborne Atmospheric Measurements (FAAM) aircraft (Hewison and English 1999; Hewison et al. 2002; Harlow 2009, 2011). These studies confirmed the large variability of

the snow, ice, and sea ice emissivities as a function of ice and snow types.

Here we propose a pragmatic approach to parameterize the snow and ice emissivities up to 700 GHz. It aims to provide realistic first-guess estimations in practical applications. It makes extensive use of the existing satellite-derived emissivities to provide realistic estimates along with reasonable spatial and temporal variabilities. It relies upon the experience already gained below 100 GHz and upon available emissivity retrievals up to 200 GHz. The methodology, the data sources, and the parameterization results are presented in section 2. The International Submillimeter Airborne Radiometer (ISMAR) instrument is a unique opportunity to document the surface emissivity above 200 GHz. It has been designed to operate at the ICI frequencies (Fox et al. 2014, 2016). It flew on the FAAM BAe-146 aircraft during two campaigns, including flights over Greenland. The snow and ice emissivity parameterizations are partly evaluated by comparison with emissivity estimation from the ISMAR observations over Greenland (section 3). Conclusions are presented in section 4.

2. Parameterization of snow and ice emissivities above 90 GHz

a. *The methodology to develop TELSEM*^{2}

The satellite-derived estimates provide realistic emissivity estimates for all continental surface types at the global scale, along with their annual dynamics. So far, consistent, long-term, and robust land surface emissivity estimates have been calculated up to 90 GHz. At higher frequencies, some datasets exist, but they need to be carefully analyzed and consolidated. As a consequence, the basis of the emissivity parameterization up to 700 GHz is our SSM/I-derived TELSEM emissivity dataset between 19 and 85 GHz (Prigent et al. 2006). From this dataset, two subsequent processing steps need to be conducted to develop the new Tool to Estimate Land Surface Emissivity from Microwave to Submillimeter Waves (TELSEM^2):

- extrapolate the dataset to higher frequencies
- provide a parameterization of the emissivity variation with incidence angle and polarization

To complement the SSM/I TELSEM emissivity database above 100 GHz, the Météo-France and the NOAA emissivity calculations up to 190 GHz help characterize the emissivity frequency dependence at high frequencies. Satellite-derived emissivities at frequencies above 100 GHz are often considered problematic, due to the increasing atmospheric contribution in the signals. However, the surface types of interest here are also the ones that are the most reliably estimated from the satellite observations, for reasons of low atmospheric water vapor contamination. The frequency dependence of the emissivities above 100 GHz is analyzed, based on a joint analysis of the SSM/I TELSEM database, the SSMIS, and the AMSU-B Météo-France estimates, and the SSMIS NOAA emissivities.

In terms of angular information above 100 GHz, SSMIS and all other imagers provide information only around 53°. For cross-track scanners such as AMSU-B, a large range of incidence angles are observed, and the statistics for a given location and angle are limited: the AMSU-B-derived emissivities are often aggregated at larger incidence angles. Météo-France provides the averaged emissivity for two ranges of angles [small angles (<30°) and large angles (>30°)], whereas in the NOAA Management Information Retrieval System (MIRS) process, the angular dependence is not provided in the final emissivity product. In terms of polarization, the cross-track scanners such as AMSU-B measure a mixed polarization. At 53°, there is an exact equal mix of vertical and horizontal polarization. Before the launch of the Global Precipitation Measurement (GPM) mission in February 2014, the only imager that measured both polarizations above 100 GHz was the Microwave Analysis and Detection of Rain and Atmosphere Structures (MADRAS) microwave imager on board the French–Indian Megha-Tropiques mission. However, it covered only the tropical latitudes and as a consequence did not observe the cold surfaces of interest here. The GPM Microwave Instrument (GMI) now provides dual-polarization measurements at 166 GHz, but work on land surface emissivities from this instrument is still to be done. The angular and polarization dependences have been carefully analyzed up to 100 GHz during the TELSEM development and a parameterization of these dependences has been suggested (see Aires et al. 2011 for more details). Here, given the lack of information, we assume that these angular and polarization dependences are also valid for higher frequencies. This is a rather crude hypothesis, but it is not possible to constrain a more realistic parameterization with the available information at this stage. Note that at Météo-France, only two angle ranges are considered (small and large angles), and that, in the NOAA/MIRS processing of the sounding instrument (i.e., AMSU-A/B and MHS), the emissivities' empirical orthogonal functions (EOFs) are assumed constant with angle for all surface types.

In the following, the satellite-derived emissivity datasets used in the development of the parameterization of the high frequency (TELSEM^2) are briefly described, and

TABLE 1. Characteristics of the satellite-derived emissivity datasets used in this analysis. Note that the NOAA/MIRS retrieves the first five EOFs with SSMIS observations. Freq. is frequency; spatial res. is spatial resolution.

Dataset	Sensor	Surface type	Freq. (GHz)	Angle, polarization	Spatial res.	Temporal sampling	Temporal cover
TELSEM	SSM/I	Continents + sea ice	19, 37, 85	53°, V + H	0.25°× 25°	Monthly mean	Climatology
Emissivity NOAA/MIRS	SSMIS	All surfaces	19, 37, 91, 150, 183	53°, V + H (<100 GHz), H (>100 GHz)	0.25°× 25°	Each satellite overpass	March + October 2014
Emissivity Météo-France	AMSU-B	Continents	89, 150, 183	Small and large angles separately, with mixed polar.	0.25°× 25°	Monthly mean	2014
Emissivity Météo-France	SSMIS	Continents	19, 37, 91, 183	53°, V + H (<100 GHz), H (>100 GHz)	0.25°× 25°	Monthly mean	2014

their consistency is evaluated for their common frequency range around 90 GHz. Then, a parameterization of the emissivity frequency dependence is proposed, for each surface type.

b. *The satellite-derived emissivity sources*

Under clear-sky conditions, assuming specular reflection, the radiative transfer equation, from either a satellite or an aircraft, can be written as

$$T_{\rm bp} = T_s \times \varepsilon_p \times e^{-\tau(0,H)/\mu} + (1-\varepsilon_p) T_d \times e^{-\tau(0,H)/\mu} + T_u. \quad (1)$$

The three terms stand for surface emission, downwelling atmospheric emission after reflection by the surface, and upwelling atmospheric emission, respectively. In Eq. (1), $T_{\rm bp}$ is the observed brightness temperature by the radiometer for polarization p; T_s is the surface skin temperature; ε_p is the surface emissivity for polarization p; τ is the atmospheric opacity; H is the sounder altitude; μ is the $\cos(\theta)$, where θ is the incidence angle; T_u is the upwelling brightness temperature from the atmospheric contribution only; and T_d is the downwelling brightness temperature at the surface. See Prigent et al. (1997) for more details.

The surface emissivity can be deduced using

$$\varepsilon_p = \frac{T_{\rm bp} - T_u - T_d \times e^{-\tau(0,H)/\mu}}{e^{-\tau(0,H)/\mu} \times (T_s - T_d)}. \quad (2)$$

Table 1 provides a summary of the satellite-derived emissivity estimates directly used in this study.

1) SSM/I-DERIVED EMISSIVITIES AND TELSEM

Our main source of information is the SSM/I-derived emissivity estimates (Prigent et al. 1997, 2006) at 19, 22, 37, and 85 GHz, calculated using ancillary data, including the International Satellite Cloud Climatology Project database (Rossow and Schiffer 1999) and atmospheric reanalysis from NOAA National Centers for Environmental Prediction (NCEP; Kalnay et al. 1996). Both orthogonal polarizations are available at 53° incidence angle (except at 22 GHz). The calculations are performed over 15 years, including the sea ice emissivities. Note that the sea ice surfaces were not included in the first version of TELSEM. The dataset is available on an equal-area grid of 0.25° × 0.25° at the equator, and monthly mean values are used here. With the help of AMSU-A- and TMI-derived emissivities, TELSEM, which is an emissivity parameterization for all incidence angles and for both orthogonal polarizations, has been developed (Aires et al. 2011).

2) SSMIS AND AMSU-B EMISSIVITIES FROM MÉTÉO-FRANCE

Based on the emissivity inversion in Eq. (2), emissivities have been calculated at Météo-France from different sensors (Karbou et al. 2006). Short-range forecast temperature and humidity profiles are used as inputs to the Radiative Transfer for the Television and Infrared Observation Satellite (TIROS) Operational Vertical Sounder (RTTOV) model to compute the atmospheric contribution to the measured radiances. In this study, we use the AMSU-B and SSMIS estimates. Calculations are performed only if the atmospheric transmission is above 0.5. The AMSU-B emissivities are calculated at 89, 150, and 183 GHz, and are averaged for both low (<30°) and high (>30°) incidence angles for a mixture of vertical (V) and horizontal (H) polarizations. The SSMIS emissivities are calculated at 53° incidence angle at 19, 37, and 91 GHz for both the V and H polarizations, and at 150 and 183 GHz for the H polarization (the instrument does not measure the V polarization at these frequencies). One year (2014) of monthly mean

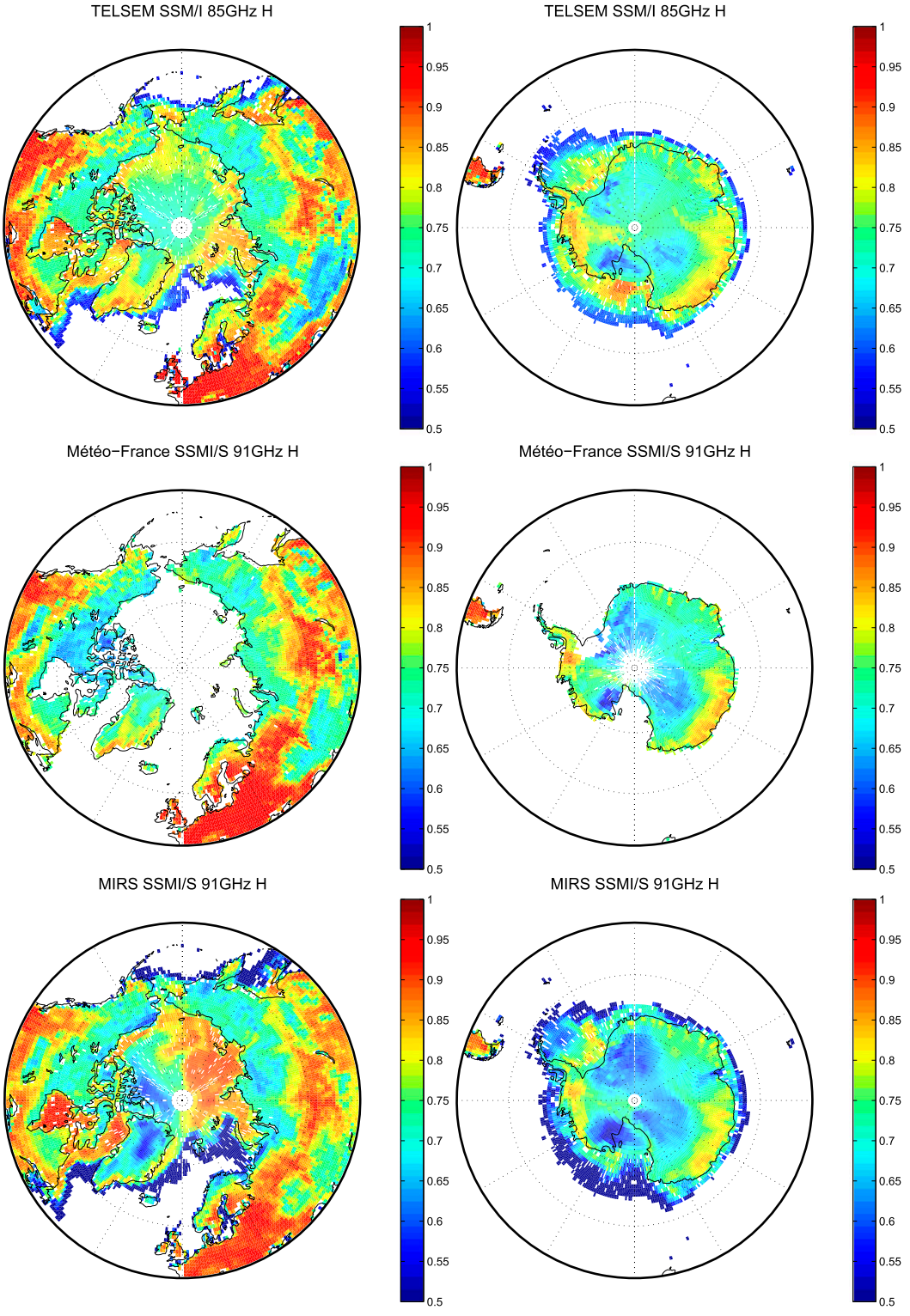

FIG. 2. The emissivity around 90 GHz at H polarization as calculated from the different groups in March, for the (left) North Pole and (right) South Pole. (top) SSM/I (85 GHz) from TELSEM, (middle) SSMIS (91 GHz) from Météo-France, and (bottom) SSMIS (91 GHz) from NOAA/MIRS.

estimates for both AMSU-B and SSMIS, with a 0.25° × 0.25° spatial resolution, has been calculated and used here. Preliminary analysis of the SSMIS dataset showed that the emissivities at frequencies greater than 150 GHz were problematic for the *F16* and *F17* satellites due to reflector emissions on these spacecraft. The *F18* spacecraft did not exhibit an emissive reflector; however, the 150-GHz channel failed, while the *F19* reflector was recoated and as a result did not exhibit this behavior (S. Swadley, NRL, 2016, personal communication).

3) SSMIS EMISSIVITY FROM NOAA/MIRS

At NOAA's National Environmental Satellite, Data, and Information Service (NESDIS), a 1DVAR retrieval algorithm named MIRS (Boukabara et al. 2011) is run to estimate the surface emissivity and the surface temperature systematically, along with the atmospheric parameters (humidity and water vapor profiles, cloud and rain quantities), from most operational microwave instruments (i.e., AMSU-A/B, MHS, and SSMIS). We concentrate on the SSMIS estimates, as it provides emissivities up to 183 GHz with a scanning angle similar to SSM/I. NOAA/MIRS retrieves the first five EOFs with SSMIS observations. The original EOF basis functions were computed offline, with separate sets for each of the four major surface types (ocean, sea ice, land, and snow-covered land) treated by NOAA/MIRS. The data are available from the NOAA's Comprehensive Large Array-Data Stewardship System (CLASS), on an orbit basis and the swath geometry. As already mentioned, the SSMIS 150- and 183-GHz channels had a known contribution from reflector emission on the *F16* and *F17* missions. However, with the NOAA/MIRS retrievals based on EOFs, some information were still extracted at this frequency, except for the *F18* mission.

4) SATELLITE-DERIVED EMISSIVITY COMPARISONS AROUND 90 GHZ OVER THE POLES

Observations around 90 GHz are available for both polarizations close to 50°, from all three groups (85 GHz from SSM/I from TELSEM, and 91 GHz from SSMIS from Météo-France and NOAA/MIRS). The frequency dependence of the emissivities being limited, the emissivities at these different frequencies are expected to be very close (Prigent et al. 2008). The consistency of the three datasets is checked in this frequency domain. Figure 2 shows the emissivities estimated around 90-GHz H polarization in March over the two poles from TELSEM, Météo-France, and NOAA/MIRS. The three emissivity datasets show very similar spatial structures (linear spatial correlation of 0.85 between TELSEM and Météo-France, and 0.76 between TELSEM and NOAA/MIRS; similar values are calculated for the V polarization). The histograms of the emissivities are presented for the same month, for the two poles, and at both polarizations, close to 90 GHz (Fig. 3). For the V polarization (H polarization), the mean difference is 0.022 (0.015) with a standard deviation of 0.025 (0.031) between TELSEM and Météo-France, and the mean difference is −0.005 (0.027) with a standard deviation of 0.053 (0.035) between TELSEM and NOAA/MIRS. Compared to the differences observed between satellite and model estimates over these surface types (mean differences of 0.048 (0.091) with a standard deviation of 0.063 (0.079) in polarization V (H); see Table 1 in Prigent et al. 2015], the differences here are limited. Part of the differences between the estimates is linked to the fact that TELSEM represents a monthly climatology and that snow and ice areas can show significant variability from one year to the other. Other differences can come from differences in surface temperature assumptions, as well as in the estimation of the atmospheric contribution.

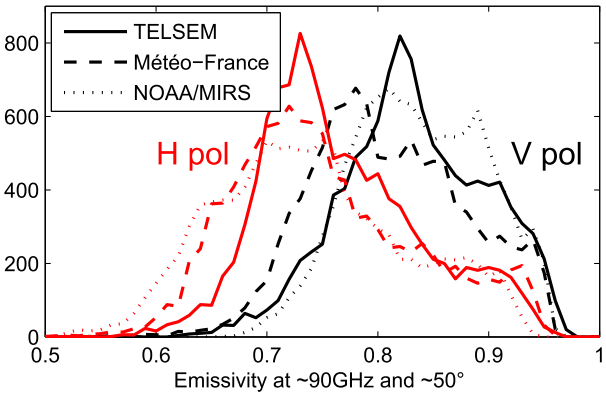

FIG. 3. Histograms of the emissivity around 90 GHz as calculated from the different groups (TELSEM, Météo-France, and NOAA/MIRS) in March over the poles for both polarizations (V in black, H in red). Sea ice surfaces are excluded.

c. *Parameterization of frequency dependence of the continental snow and ice emissivity*

The emissivities of continental snow and ice have been estimated by all three groups (TELSEM, Météo-France, and NOAA/MIRS). To ease the analysis of the frequency dependence, the continental snow and ice emissivities from TELSEM (from 19 to 85 GHz) are classified, using a *k*-mean method with six classes. The result of the classification is presented in Fig. 4 for January and July. Note that the classes have been ordered, to provide some continuity from a class to the

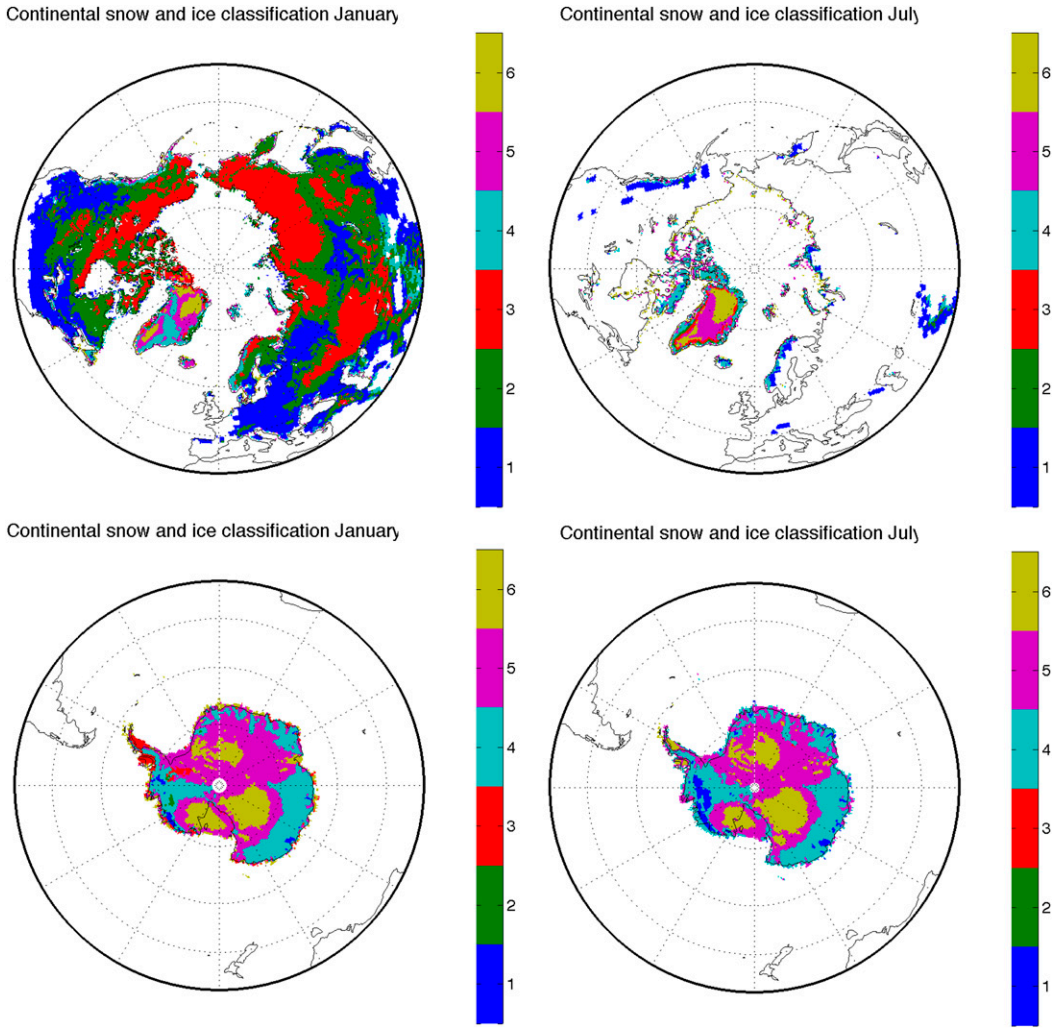

FIG. 4. Results of the continental snow and ice emissivity *k*-mean classification from SSM/I TELSEM over the (top) North Pole and (bottom) South Pole in (left) January and (right) July. Six classes are used.

next, and to facilitate the interpretation. Classes 1–3 correspond mainly to snow regions, whereas classes 4–6 are essentially present over continental ice in Antarctica and Greenland. There are limited changes from January to July in Antarctica, slightly more in Greenland. The corresponding frequency dependence for each class is indicated in Fig. 5 (in black). Classes 1–3 show a decrease of the emissivity with frequency, related to increasing scattering in the snowpack. From classes 1 to 3, snow is getting dryer and thicker, with increasing snow grain size. Class 1 is located mostly around the midlatitudes, where the snow can be wet and shallow. Class 3 corresponds to very dry and thick snowpack, with large grain sizes that induce strong scattering around 90 GHz. For classes 4–6, the emissivities tend to increase with frequency, especially for the H polarization. A detailed analysis of the sensitivity of the emissivity to the snow parameters has been proposed by Cordisco et al. (2006) based on the SSM/I-derived emissivities as well.

The frequency dependence of the emissivity is now compared to the results from Météo-France and NOAA/MIRS emissivity estimates. For each month, each location belongs to a class following the climatologically based TELSEM classification. The NOAA/MIRS and Météo-France emissivities are grouped by classes, based on only their geographical location and month, following the TELSEM classification. The averaged frequency dependence per class is calculated and shown in Fig. 5, for the three databases. The SSMIS and SSM/I estimates correspond to the same geometry (53° incidence angle), and SSMIS measured only the H polarization at high frequencies. For the AMSU-B estimates, an average of all large angles (>30°) and an average of the V and H polarizations (the

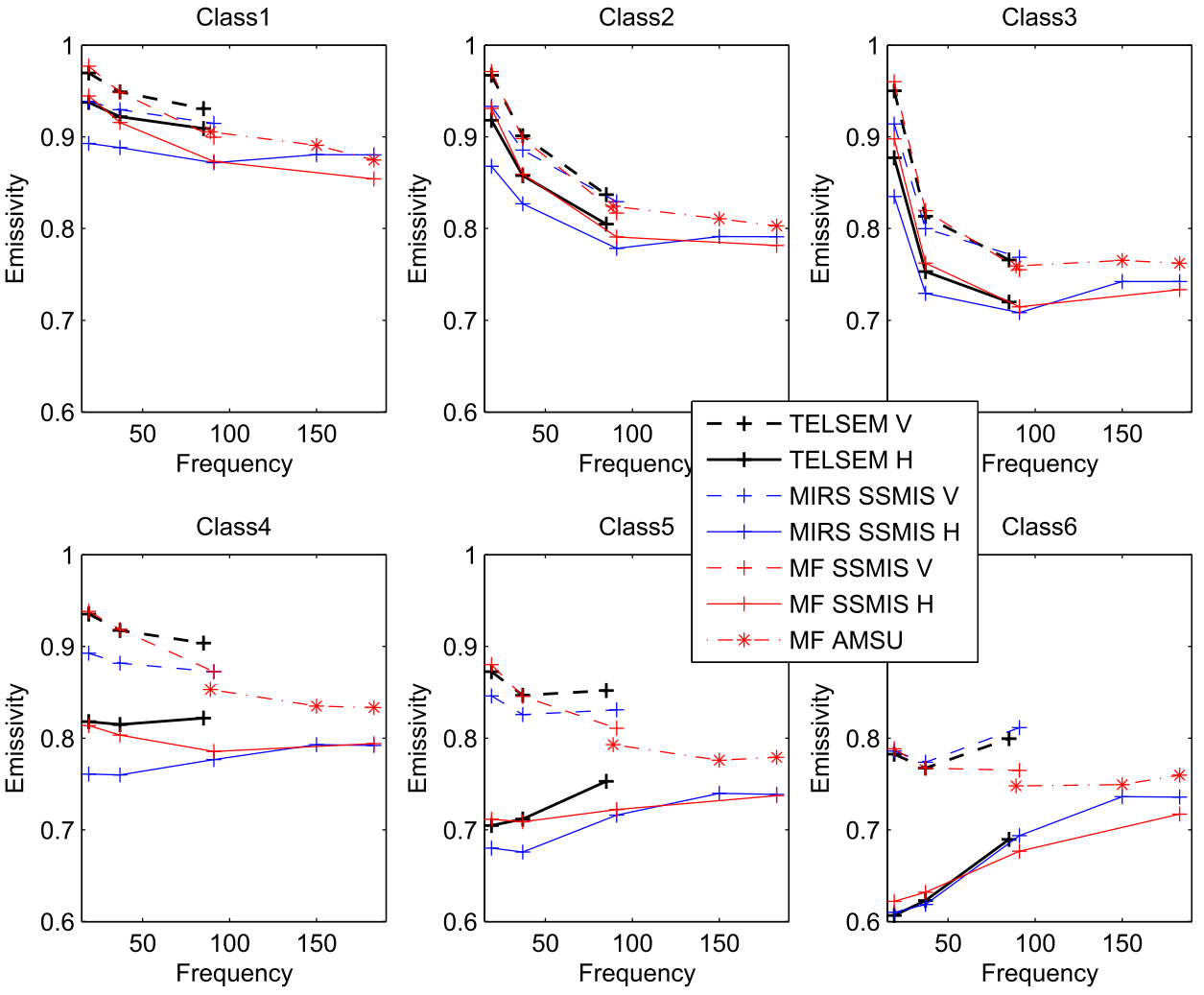

FIG. 5. Frequency dependence of the snow and ice emissivities, for different classes, for SSM/I TELSEM, SSMIS NOAA/MIRS, and AMSU-B and SSMIS Météo-France.

case for 53° incidence angle) are presented here. The results show a very similar frequency dependence for TELSEM and NOAA/MIRS up to 90 GHz, but with a significantly lower value of NOAA/MIRS with respect to TELSEM for both polarizations (larger for the H polarization), for all classes except class 6, where the agreement is quite good. The SSMIS Météo-France estimates are very close to SSM/I TELSEM estimates at 19 and 37 GHz, but for most classes, the estimates around 90 GHz differ significantly, with lower emissivities obtained with SSMIS. The 89-GHz AMSU-B estimates from Météo-France are very close to the SSMIS estimates at V polarization from both Météo-France and NOAA/MIRS. This is not expected, since it should be close to the average of the V and H polarizations. For classes 4–6, the 89-GHz AMSU-B estimates are very close to the average of the V and H polarizations of the SSM/I TELSEM emissivities. The SSMIS estimates from NOAA/MIRS and Météo-France agree reasonably well around 90 and 183 GHz, with a rather limited frequency dependence between these two frequencies. Part of the differences in behaviors is due to the time mismatch between these datasets: TELSEM is a monthly mean climatology over 15 years, whereas Météo-France and NOAA/MIRS are representative of one year (2014). Other sources of discrepancies can come from the differences in the surface temperature used by the emissivity estimates, the differences in the water vapor, and calibration issues between the instruments. In addition, the TELSEM and Météo-France emissivities are representative of clear-sky scenes only, whereas NOAA/MIRS processes all pixels, clear and cloudy. From this analysis, it is concluded that the frequency

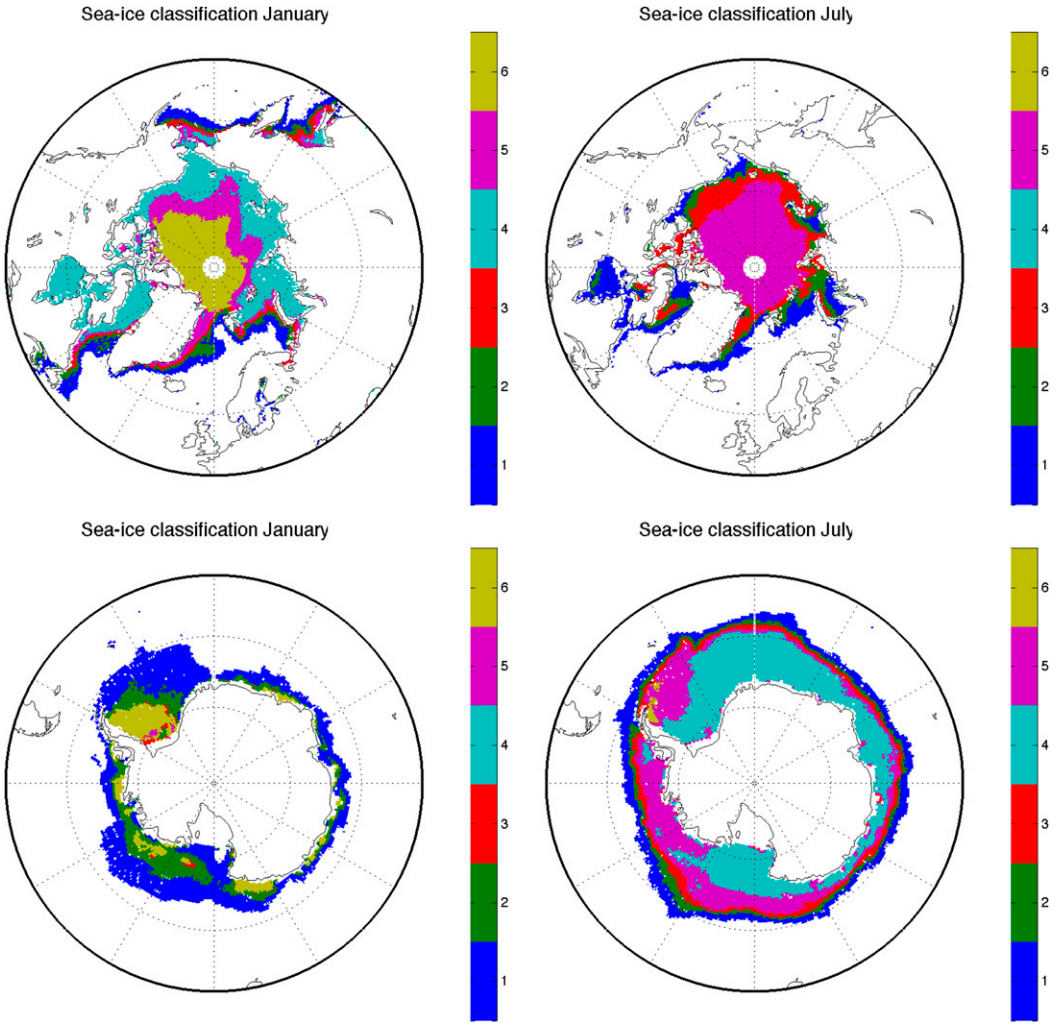

FIG. 6. Results of the sea ice emissivity classification from SSM/I TELSEM over the (top) North Pole and (bottom) South Pole in (left) January and (right) July.

dependence of the continental snow and ice emissivities is limited, and the emissivities are assumed constant for frequencies above 85 GHz (equal to the 85-GHz emissivity) for both the V and H polarizations.

d. Parameterization of the frequency dependence of the sea ice emissivity

Depending on its type (new ice, first-year ice, or multiyear ice), sea ice exhibits various emissivity behaviors, related to differences in dielectric and scattering properties. With age, the ice thickness increases, its salinity decreases, and the potential snow cover changes. These sea ice emissivities were not included in the first version of TELSEM, and the database is first updated to add the sea ice component. The presence of sea ice is derived from the National Snow and Ice Data Center (NSIDC) analysis. Similar to the treatment of the continental snow and ice, a classification is applied to the monthly mean climatological emissivities, with a *k*-mean classification with six classes. The result of the classification is presented in Fig. 6 for the two poles in January and July.

Over sea ice, the Météo-France emissivity estimates are not available above 100 GHz, so we rely on the SSMIS NOAA/MIRS estimates for the frequency extrapolation of the emissivities. The SSMIS NOAA/MIRS emissivities are grouped by class, following the SSM/I TELSEM classification for each location and month (as for continental snow and ice). The averaged frequency dependence per class is calculated and shown in Fig. 7, as compared to the SSM/I TELSEM results (only the H polarizations are measured at high frequencies with SSMIS). Class 1 corresponds to the presence of new sea ice likely mixed with open water:

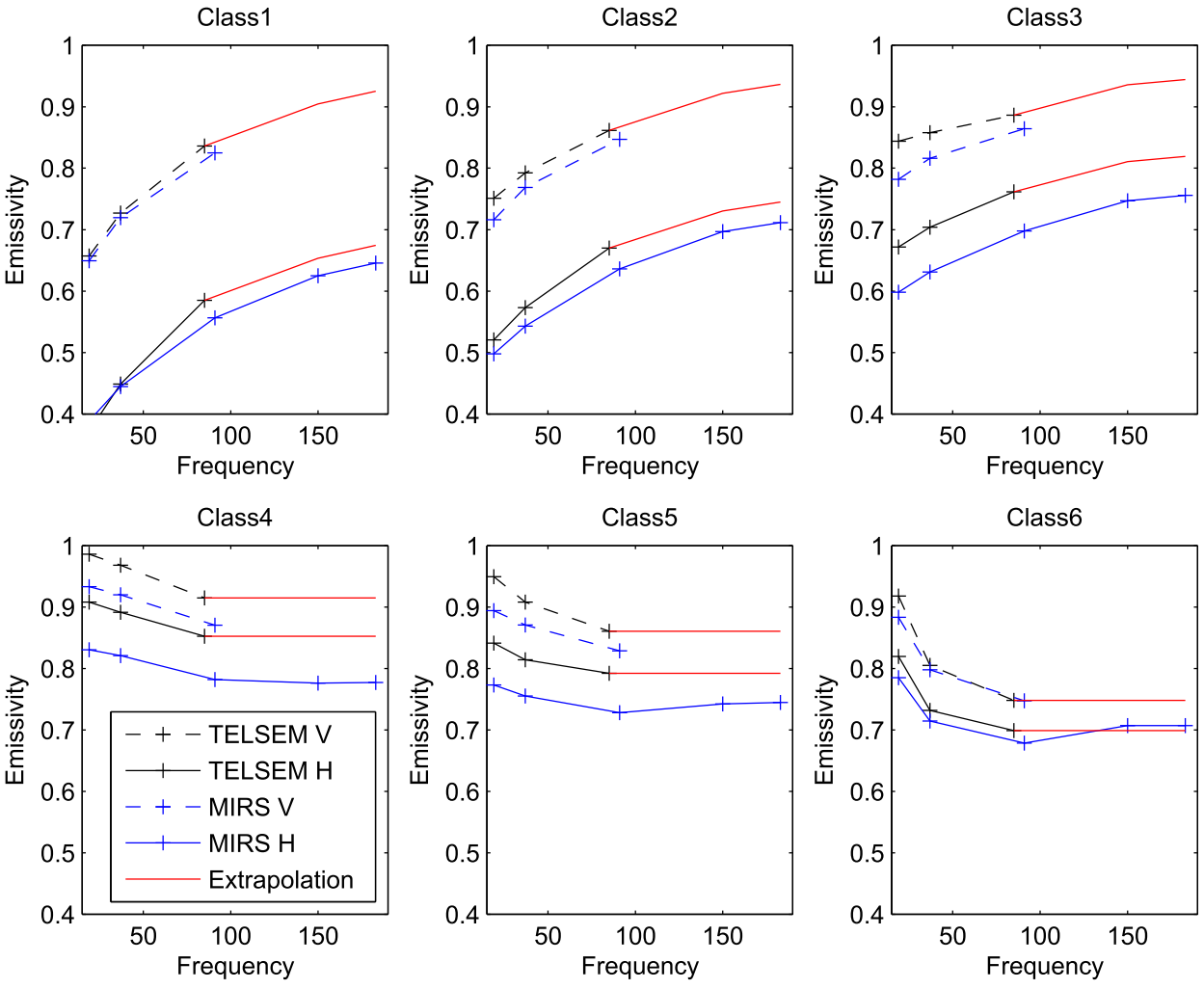

FIG. 7. Frequency dependence of the emissivity per sea ice class, for both V and H polarizations, from SSM/I TELSEM (black) and SSMIS NOAA/MIRS (blue). The suggested extrapolation of the SSM/I TELSEM is indicated in red.

it is associated with low emissivities at low frequencies, the emissivity increases with frequency, and this class is present at the ice edge. Classes 2 and 3 are also associated with recent ice, with increasing emissivities at low microwave frequencies. The three other classes have very different emissivity behaviors, with rather high emissivities at low frequencies and decreasing emissivities with frequencies within this frequency range. These classes are located closer to the poles. The emissivity decrease with increasing frequency is related to scattering mechanisms over large particles. One immediately notices that there are significant systematic differences between the SSM/I and the SSMIS results, with the SSMIS emissivities generally lower than the SSM/I TELSEM emissivities. However, it is very reassuring to observe that the frequency dependences are very similar for the two estimates below 100 GHz, with close to parallel behaviors in frequencies for both polarizations. The first three classes show a monotonic increase of the emissivity with frequency. For classes 5 and 6, the emissivities decrease below 90 GHz but increase slightly after 90 GHz. This behavior has also been observed from aircraft measurements over multiyear ice (see Hewison and English 1999). As stated above, MIRS can retrieve an emissivity at 150 GHz via EOF with the information at 89 and 183 GHz, even if there is no measurement (bad channel). Whether it should actually be used in this case is questionable, since the retrieval cost function will not include any radiometric penalty term at 150 GHz.

To provide an idea of the variability of behaviors in the SSMIS dataset, Fig. 8 presents the frequency dependence of a few randomly selected pixels in the

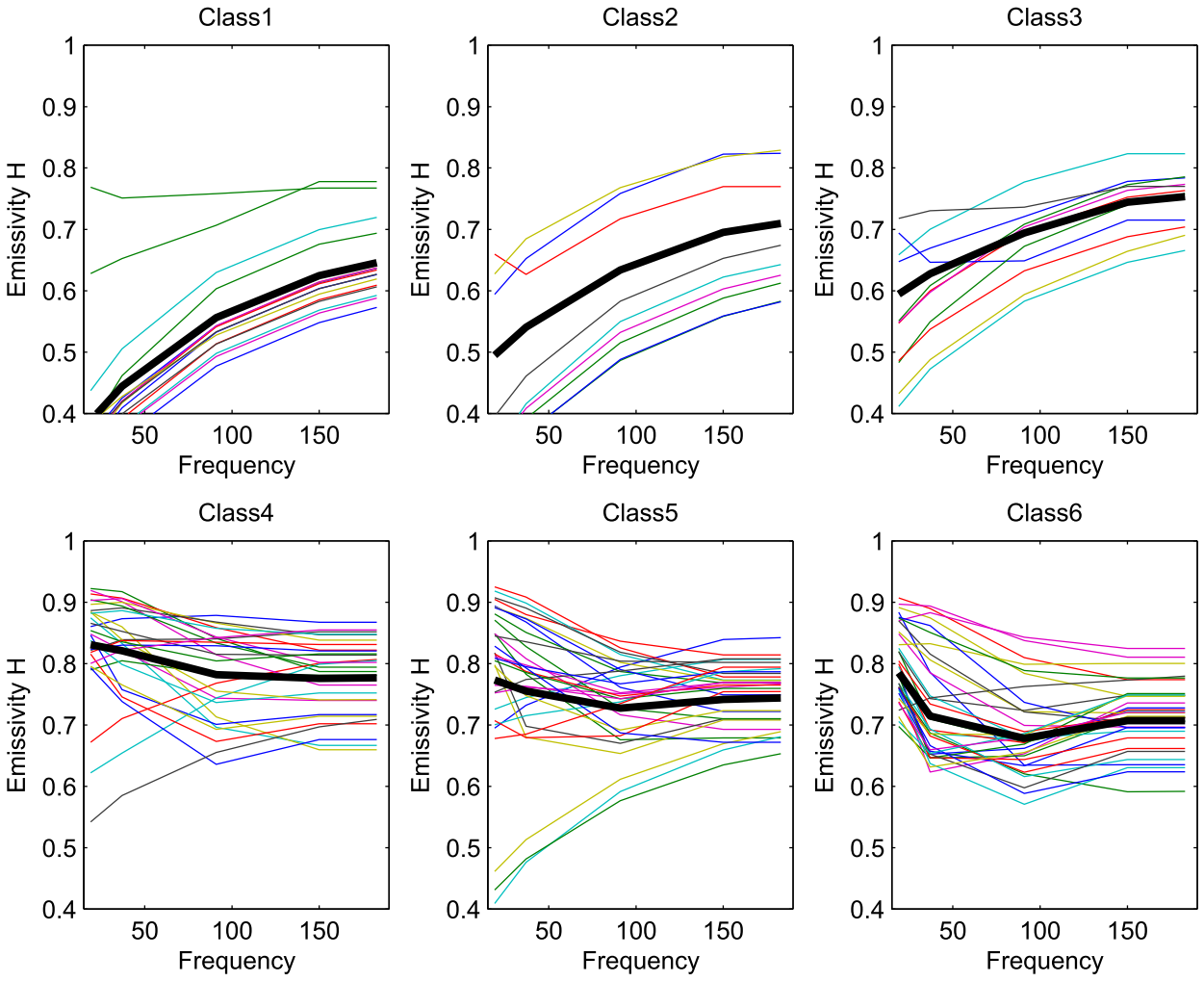

FIG. 8. Frequency dependence of the SSMIS NOAA/MIRS emissivities, for a few randomly selected pixels per sea ice class (for H polarization only, as V polarization is not available at high frequencies). The mean behavior is indicated with a thick black line.

database for each class. The mean behavior as obtained above is also added (thick solid black line). As expected, there is a significant variability of behavior within a class as specified by the SSM/I TELSEM climatology, but there is nevertheless a rather good consistency within a class. Because of factors such as matching instantaneous values to a climatology, some pixels are clearly assigned to the wrong class, this can be seen in many of the pixel groupings, such as classes 4 and 5.

As a consequence, for the extrapolation of the emissivities in frequency, we suggest adopting different strategies for the first three classes and for the last three ones. For the first three classes, we propose to adopt the same frequency dependence as the one obtained with SSMIS, corrected from the bias around 85 GHz. In the absence of any information for the V polarization, the same frequency dependence is applied to both V and H polarizations: this is also justified by the rather parallel behavior of the two polarizations between 37 and 85 GHz. For these first three classes, the ratio of the emissivity versus frequency slopes between 150 and 85 GHz and between 85 and 37 GHz is assumed constant for a given class, as well as the ratio of the emissivity versus frequency slopes between 183 and 150 GHz and between 150 and 85 GHz. This hypothesis appears to be a reasonable and pragmatic approach at this stage, considering the limited information at our disposal. Above 183 GHz, the emissivity is assumed constant with frequency. Occasionally in the database, the emissivity does not increase with frequency between 37 and 85 GHz for these three classes. In these cases, the emissivity is assumed constant above 85 GHz. For the last three sea ice classes, the frequency dependence above 100 GHz is limited, and a conservative approach is adopted: the emissivities are

TABLE 2. Channel characteristics of the ISMAR and MARSS instruments, including their frequencies, bandwidth (BW), instrument noise (measured NetΔT on liquid nitrogen–cooled target over 60 s, from Fox et al. 2016), polarization, field-of-view (FOV) angle (full width at half maximum), and main spectral features. The polarizations indicated here are the polarizations in the +50° downward view for all the channels. The Microwave Imager (MWI) is an instrument on board the MetOp-SG as ICI.

Instrument (GHz)	Center freq. (GHz)	Freq. offset (GHz)	BW (GHz)	NetΔT (K)	Polarization	FOV (°)	Spectral feature
MARSS (MWI)	89	± 1.1	0.65	0.42	Mixed	12.0	Window
5 × ISMAR (MWI)	5 × 118.75	± 1.1	0.4	0.4	5 × V	5 × <3.8	5 × O_2
		± 1.5	0.4	0.4			
		± 2.1	0.8	0.3			
		± 3.0	1.0	0.3			
		± 5.0	2.0	0.3			
MARSS (MWI)	157.0	± 2.6	2.6	0.69	H	11.0	Window
3 × MARSS (ICI)	3 × 183.31	± 1.0	0.45	0.64	3 × H	3 × 6.2	3 × H_2O
		± 3.0	1.0	0.44			
		± 7.0	2.0	0.35			
2 × ISMAR (ICI)	2 × 243.2	± 2.5	3.0	0.3	V	2 × <3.6	2 × window
				0.4	H		
3 × ISMAR (ICI)	3 × 325.15	± 1.5	1.6	1.6	3 × V	3 × <3.6	3 × H_2O
		± 3.5	2.4	0.7			
		± 9.5	3.0	1.1			
3 × ISMAR (ICI)	3 × 448.0	± 1.4	1.2	1.1	3 × V	3 × <3.6	3 × H_2O
		± 3.0	2.0	1.6			
		± 7.2	3.0	2.8			
2 × ISMAR (ICI)	2 × 664.0	± 4.2	5.0	3.3	V	2 × <3.8	2 × window
				1.3	H		

assumed constant with frequencies above 85 GHz. The resulting extrapolation is presented in red in Fig. 7 for each class.

3. Evaluation of the emissivity parameterization with airborne observations

The ISMAR instrument has been tested and operated in two field campaigns out of Prestwick, Scotland, on December 2014 and March 2015, on board the FAAM BAe-146 research aircraft. The Microwave Airborne Radiometer Scanning System (MARSS) complements the ISMAR on board this aircraft, with channels at 89, 157, and 183 GHz.

The emissivity can be directly calculated from the ISMAR and MARSS observations for each frequency, polarization, and scan angle with Eq. (2), taking into account the atmospheric contribution and the surface temperature. The airborne-derived emissivities are compared to the new emissivity parameterization TELSEM^2. We are fully aware of the limited scope of the exercise, with only a few flights available, and limited atmospheric and surface conditions.

a. The aircraft radiometers

ISMAR is an along-track scanning radiometer with five channels in the oxygen line at 118.75 GHz, three channels near the water vapor lines at 325.15 and 448 GHz, and two window channels at 243.2 and 664 GHz. The two window channels have two orthogonal polarizations that rotate with scan angle, giving both V and H polarizations in the +50° downward view. It is the same for the other channels, but only V polarization is given in the +50° downward view (Fox 2015; Fox et al. 2016). The instrument is calibrated against two blackbody targets, one at ambient temperature and the other one heated. The instrument viewing angles are between +55° and −10° downward and between +10° and −40° upward.

MARSS is also an along-track scanning radiometer. It observes in five channels corresponding to AMSU-B, including two window channels (89 and 157 GHz) and three channels near the water vapor line (183.31 GHz). Each scan takes 3 s, with scene views from −40° to +40°, and two views of the blackbody targets. A single linear polarization is measured in each channel, and the polarization rotates with scan angle. See Hewison (2006) for more details. The channel specifications for both instruments are listed in Table 2.

b. The COSMICS campaign

The Cold-Air Outbreak and Submillimeter Ice Cloud Study (COSMICS) campaign took place between 4 and 25 March 2015 from Prestwick with fights up to Greenland. Two flights (B896 and B898) from this campaign are of special interest for emissivity calculations over snow and ice: they provide level runs suitable for surface emissivity calculation, under dry and rather

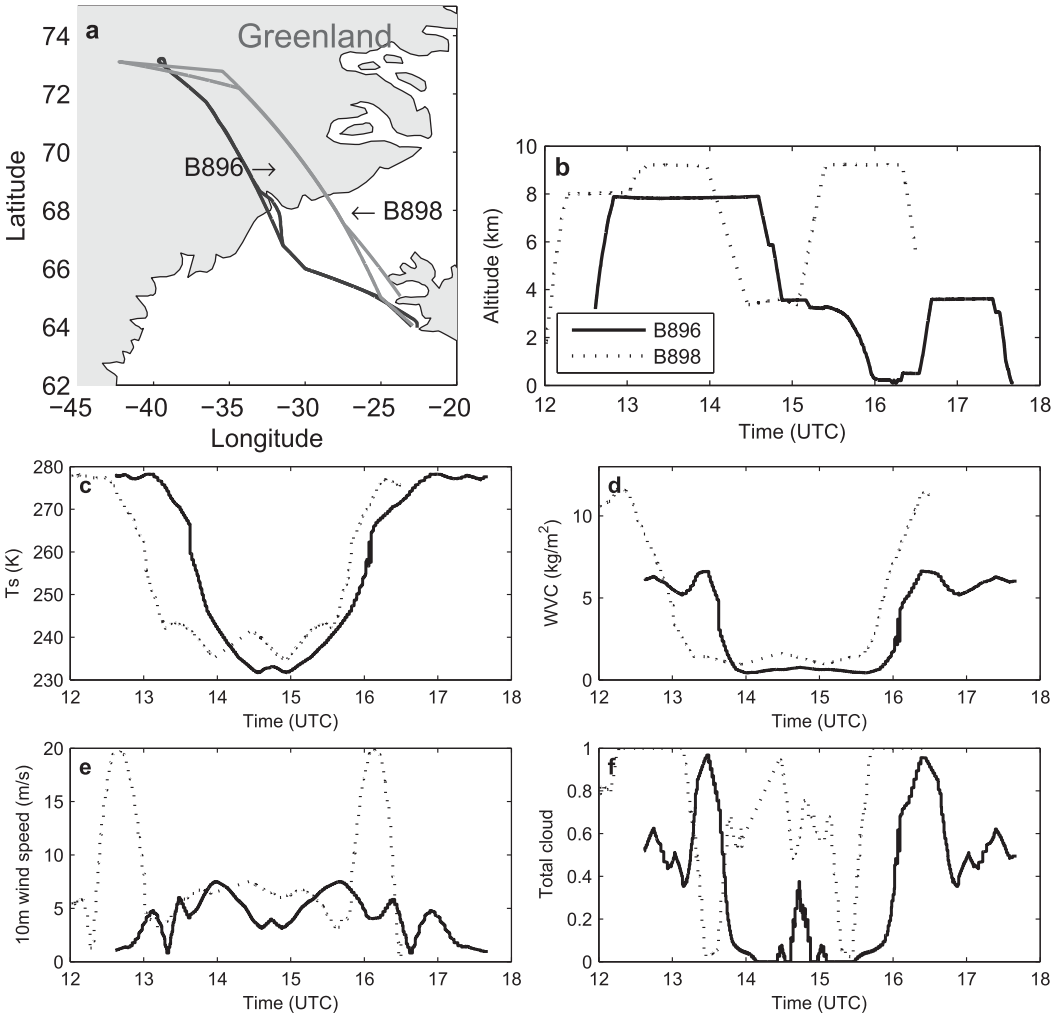

FIG. 9. (a) The flight track of flights B896 (black) and B898 (gray) back and forth from Greenland. (b) The flight altitudes as a function of the observation time. (c) The surface skin temperature, (d) integrated water vapor content, (e) 10-m wind speed, and (f) fraction of total cloud from the ERA-Interim database as a function of the observation time during these two flights. Flight B896 (B898) started from island at 1237 (1201) UTC, reached its destination at 1447 (1430) UTC, and came back to the island at 1741 (1630) UTC.

clear conditions. The two flights started from Iceland and aimed at the Greenland summit, with B898 east of B896. Figure 9 indicates the two flight patterns and the flight altitudes. The atmospheric background during these flights is also presented in Fig. 9. The Greenland surface temperature was around 230 K, and the water vapor content was less than 1 kg m^{-2}.

Figures 10 and 11 present the observed brightness temperatures (TBs) at zenith and nadir, respectively, for flight B896, along with corresponding radiative transfer simulations. From Iceland to Greenland, flight B896 overpassed sea ice on its way toward the Greenland summit and then flew back to Iceland (Fig. 9). The aircraft flew much closer to the surface on its way back to Iceland. Some clouds were present during that flight (Fig. 9), with some expected effects, especially at high frequencies. Note that, according to the lidar measurements during this flight (not shown), ERA-Interim was overestimating cloud cover: it was clear over the summit plateau, as well as during flight B898. For B896, there was no cloud presence below the aircraft between 13.8 h (~68.5°N) and 16.2 h (close to the coast). For B898, there was high cloud below the aircraft until about 13.3 h (69.5°N), after which it was clear until 15.4 h (70°N). The atmospheric radiative transfer is simulated with ARTS (Eriksson et al. 2011). The Rosenkranz (1998) and Rosenkranz and Staelin (1998) models are selected for water vapor and oxygen, respectively. The atmospheric profiles are extracted from the closest in space and time ERA-Interim profiles at 0.125° × 0.125° spatial

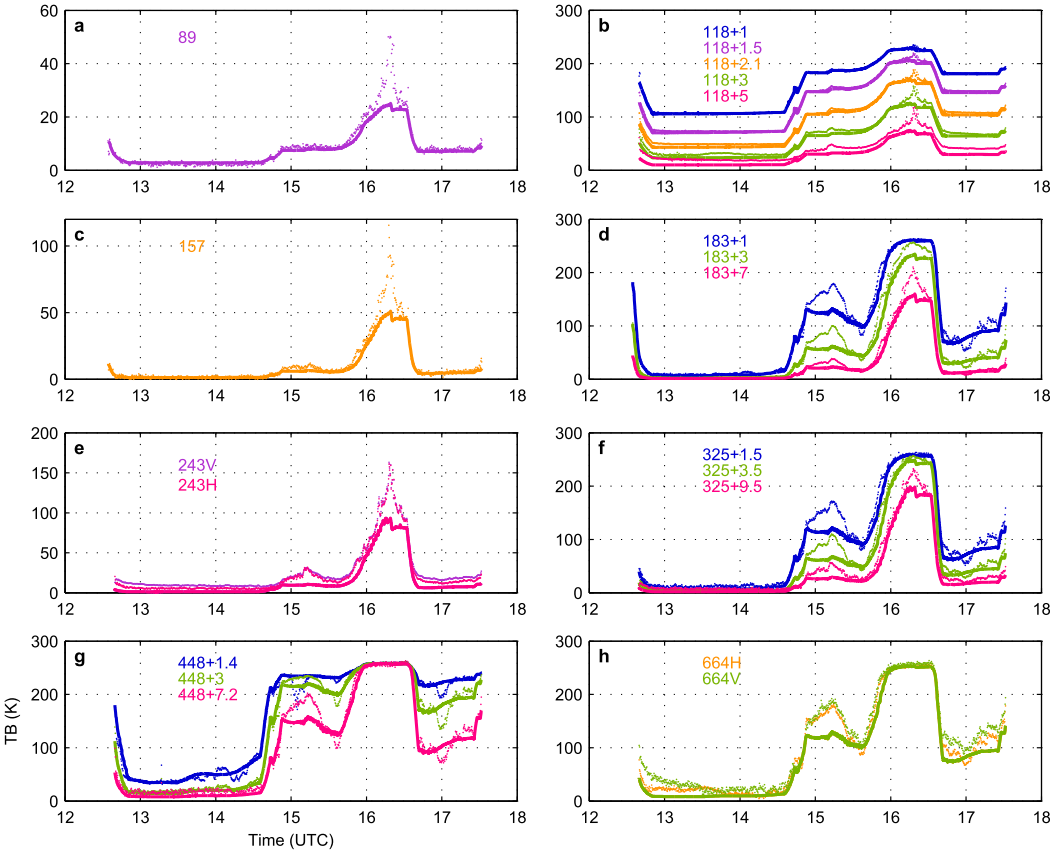

FIG. 10. The ISMAR and MARSS upward TB observations for all channels as a function of the observation time for flight B896 at zenith (dotted lines). The TB simulations by ARTS are also presented (solid lines). Flight B896 started from Greenland at 1237 UTC, reached its destination at 1447 UTC, and came back to the island at 1741 UTC.

resolution. The pitch, roll, and orientation angles of the aircraft are taken into consideration in the simulations. A clear-sky condition is assumed for all the simulations.

In general, the upward-looking simulated and observed brightness temperatures are in rather good agreement, although there are some discrepancies (Fig. 10). Between 16.2 and 16.5 h, the aircraft was close to the surface, and the differences are likely due to cloud presence above the aircraft, which is not included in the simulations. This effect is less pronounced in channels close to the center of the absorption lines and at much higher frequencies (448 and 664 GHz) where the atmosphere is opaque and radiates at a similar temperature to the cloud. Between 15 and 15.4 h, the differences are larger in channels sensitive to water vapor absorption and are thought to be caused by errors in the ERA-Interim water vapor profile used in the simulations. Note that neither of these discrepancies will affect the retrieval of emissivity during low-level flight, since the observed downwelling brightness temperature is used in Eq. (2). At 243.2 GHz, the observations are warmer than the simulations, particularly at high altitudes, and there is some difference between the two polarizations, which is not expected under clear-sky conditions. A similar effect is seen in the oxygen absorption band at 118 GHz, where the difference between the model and simulation increases when moving away from the absorption line center. These differences are thought to be caused by detector nonlinearity, but they should not significantly affect the emissivity retrievals, as they are most pronounced at high altitudes where the downwelling brightness temperature at the surface is dominated by emission from the atmosphere between the aircraft and the surface.

For the downward-looking views (Fig. 11), a large spatial variability is noticed up to ~14 h. This corresponds to the overflying of coastal regions with large spatial variability (sea ice, fjord, and mountainous areas). After 14 h, the aircraft overflew the Greenland Plateau and the TBs are smoother, especially at window frequencies. The downward-looking TBs have been simulated with two assumed surface emissivities: 0.5 and

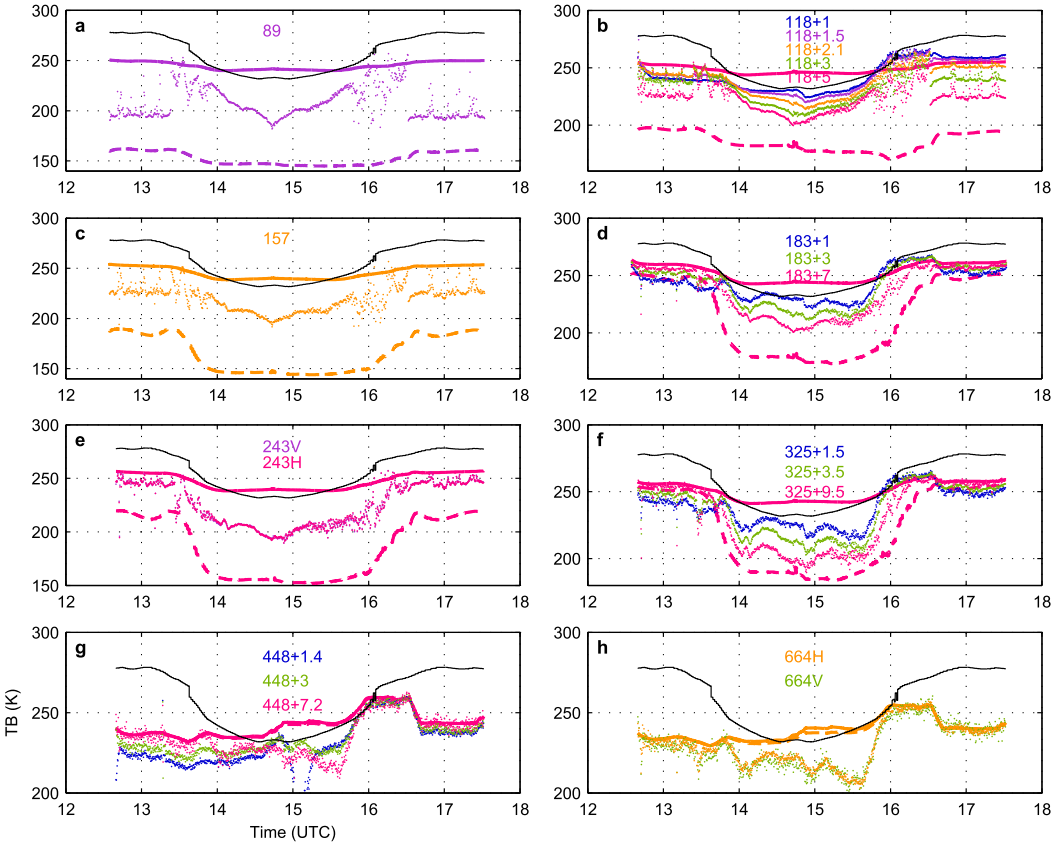

FIG. 11. The ISMAR and MARSS downward TB observations for all channels as a function of the observation time for flight B896 at nadir (solid lines). The TB simulations are also presented for the window channels for a fixed surface emissivity of 0.5 (dashed lines) and 0.9 (solid lines). The surface skin temperatures from the ERA-Interim database are indicated in black. Flight B896 started from Greenland at 1237 UTC, reached its destination at 1447 UTC, and came back to the island at 1741 UTC.

0.9. At 448 GHz and above, it is evident that there is no sensitivity to the emissivity, both on the way to and from Greenland: the two simulations of the down-looking TBs are identical, despite the large difference in emissivity. As a consequence, it is not possible to estimate the emissivity from the observations at 448 GHz and above.

c. *Emissivity calculation over Greenland from the aircraft observations and comparison with TELSEM*^{2}

In the case of the aircraft observations, in Eq. (2), $T_{\rm bp}$ is the upward brightness temperature measured by ISMAR or MARSS. The downwelling brightness temperature T_d is calculated at the surface using a combination of the upward-looking aircraft observations down to the aircraft altitude and simulations based on ERA-Interim database below the aircraft. The upwelling brightness temperature T_u and the upwelling atmospheric emission τ are estimated with ARTS, using the ERA-Interim database. The surface temperature T_s is taken from the ERA-Interim database. For flight B896, T_s has been estimated from aircraft instrumentation at the Met Office: the emissivity calculations are tested with these different T_s.

The TELSEM^2 estimates are systematically compared to the aircraft-derived emissivities. The only inputs to TELSEM^2 are the latitude and longitude of the point, the month of observation, and the observing conditions (frequency, incidence angle, and polarization). Figure 12 presents the TELSEM^2 emissivities in the region for frequencies up to 325 GHz, at 40° for both sea and continental ices, along with the flight patterns for B896 and B898. The TELSEM^2 emissivity shows a significant spatial variability, especially close to the coast both over sea and continental ices. This is to be compared with the aircraft observations, keeping in mind that the spatial resolution of TELSEM^2 is poor compared to the aircraft footprint. In these areas of marginal sea ice on March and in coastal region with significant topography, the comparison is expected to be challenging.

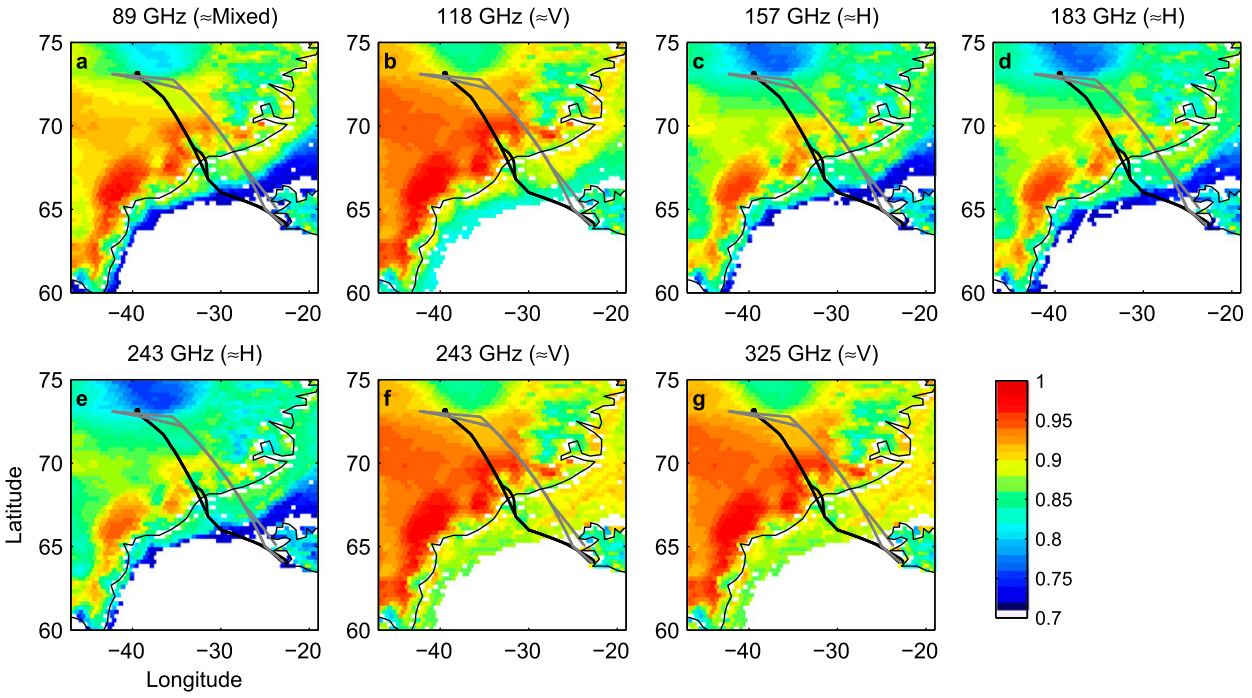

FIG. 12. B896 (black) and B898 (gray) flight patterns back and forth from Greenland, superposed onto the TELSEM^2 emissivities estimated at 40° for ISMAR and MARSS frequencies up to 325 GHz, for both sea and continental ices. The polarizations indicated in the titles are the polarizations in the +50° downward view for these channels.

Figure 13 shows the aircraft-retrieved emissivities at 0°, as a function of latitude for the window channels (89, 157, and 243 GHz) and the channels farthest from the absorption line centers (118 ± 5, 183 ± 7, and 325 ± 9.5 GHz). The top (bottom) two rows present the emissivities calculated on the way to (from) Greenland. Sea ice is present from 67° to 68°N in latitude; the rest of the transect is over continental ice. The TELSEM^2 emissivities are also presented for comparison, for the same frequencies, incidence angles, and polarizations. Over sea ice (from 67° to 68°N), the aircraft-retrieved emissivities show a very large variability. On the way to Greenland, it is likely due to the natural spatial variability of the sea ice that is expected to be high, but on the way back from Greenland, a poor temperature separation between the calibration targets is suspected, inducing an increased noise in the retrievals during this section of the flight. At 325 GHz, the estimates between 67° and 68.5°N are very noisy, especially on the way back from Greenland: this is due to the lack of sensitivity to the emissivity in this region (see the simulations in Fig. 11, with the two different emissivities, 0. 5 and 0.9, that provide very similar brightness temperatures). Over continental ice, from 69° to 73°N, the agreement between the TELSEM^2 and the aircraft estimates is good at 89 GHz but degrades at higher frequencies. Beyond 71°N, the differences between the aircraft retrievals and TELSEM^2 may be induced by two reasons. The first reason may be related to the errors in ERA-Interim water vapor profile as discussed in Fig. 10. The second one maybe related to our hypothesis made in TELSEM^2, assuming that the surface emissivity is constant at frequencies higher than 90 GHz. Beyond 71°N, the region is associated with class 5 (continental ice). The emissivity increases slightly between 89 and 183 GHz for H polarization (see Fig. 5). Therefore, it is possible that TELSEM^2 underestimates the surface emissivity for this type of continental ice between 89 and 183 GHz. In addition, some spatial structures in the emissivity retrieval that are visible at 70°N at 243 GHz are clearly not present at 89 GHz, either in the emissivity retrieval or in the TELSEM^2 estimates. This could be related to some specific snow and ice conditions that would induce emissivity changes at higher frequencies. These signatures are missed by TELSEM^2, which is anchored to emissivity estimates below 100 GHz, with limited reliable satellite-derived emissivity retrievals at frequencies above 100 GHz. Overall, the spatial variability is captured by TELSEM^2, despite the fact that TELSEM^2 is based on a monthly climatology.

Over ice (sea and continental), the surface temperature is subject to large errors, which will cause errors in emissivity retrieval. The Met Office retrieved and

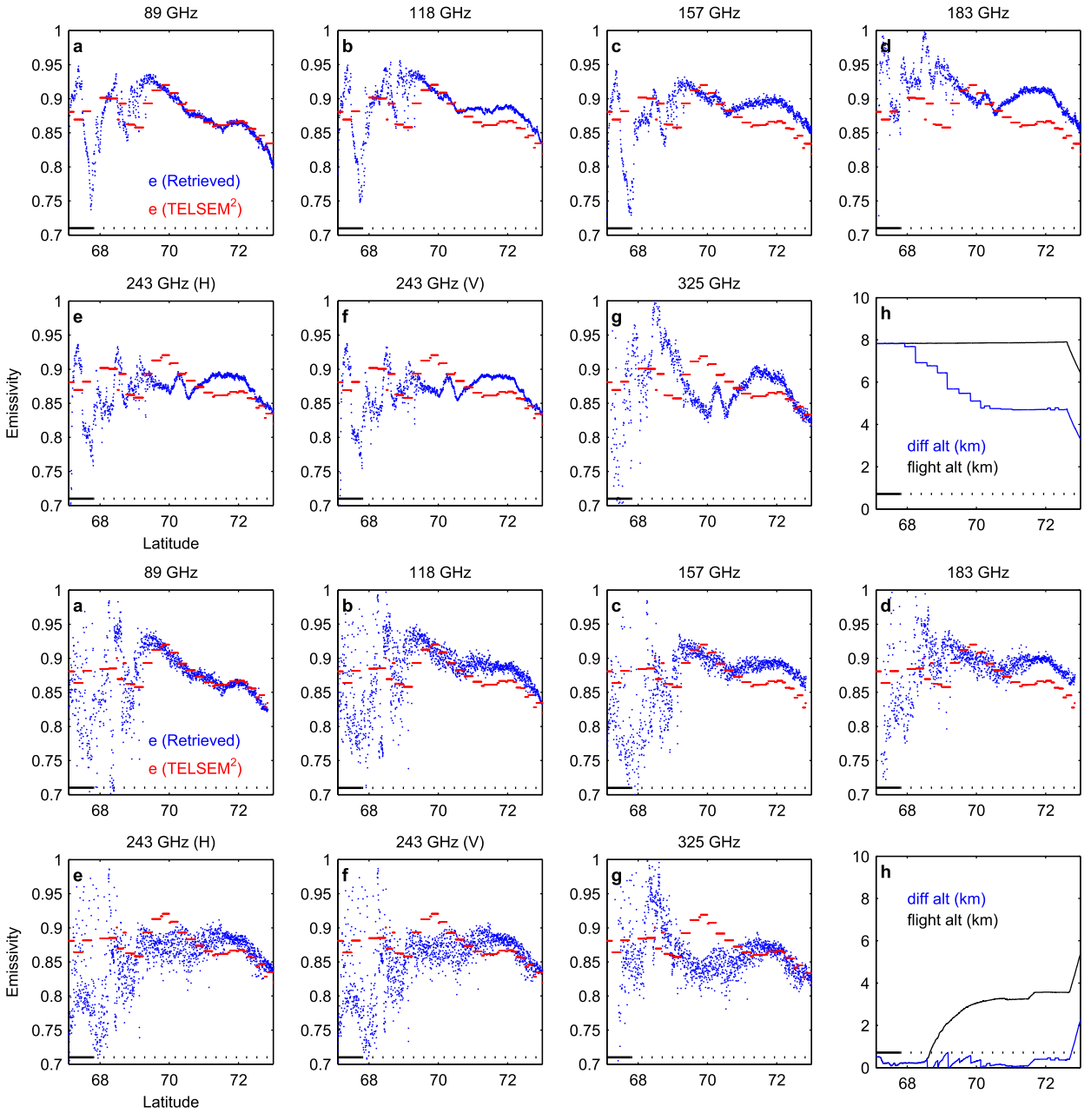

FIG. 13. The retrieved emissivity from MARSS and ISMAR observations for flight B896 as a function of latitude at 0° scan angle for 89, 118 ± 5, 157, 183 ± 7, 243, and 325 ± 9.5 GHz. (top two rows) on the way to Greenland. (bottom two rows) On the way back from Greenland. The results from TELSEM^2 in March at 0° are shown for comparison. (h, top) The flight altitude and (h, bottom) the altitude difference between the aircraft and the surface. On the x axis, the solid black line indicates the presence of sea ice and the dotted line corresponds to the continent.

analyzed the surface temperature estimated by several methods, directly from the aircraft estimates for flight B896. It includes infrared retrieval from the Advanced Remote-Sensing Imaging Emission Spectrometer (AIRES; Wilson et al. 1999), as well as estimates from an infrared Heimann sensor. Figure 14 shows the results from this work on the way from Greenland. Notice the large T_s gradient between 68° and 70°N, along with the large difference between the aircraft estimates and the ECMWF T_s. This is likely partly related to the spatial resolution differences between these estimates, in an area of large spatial heterogeneity (fjords and mountains). The T_s differences can be large between the T_s estimates, up to 10 K even between aircraft estimates.

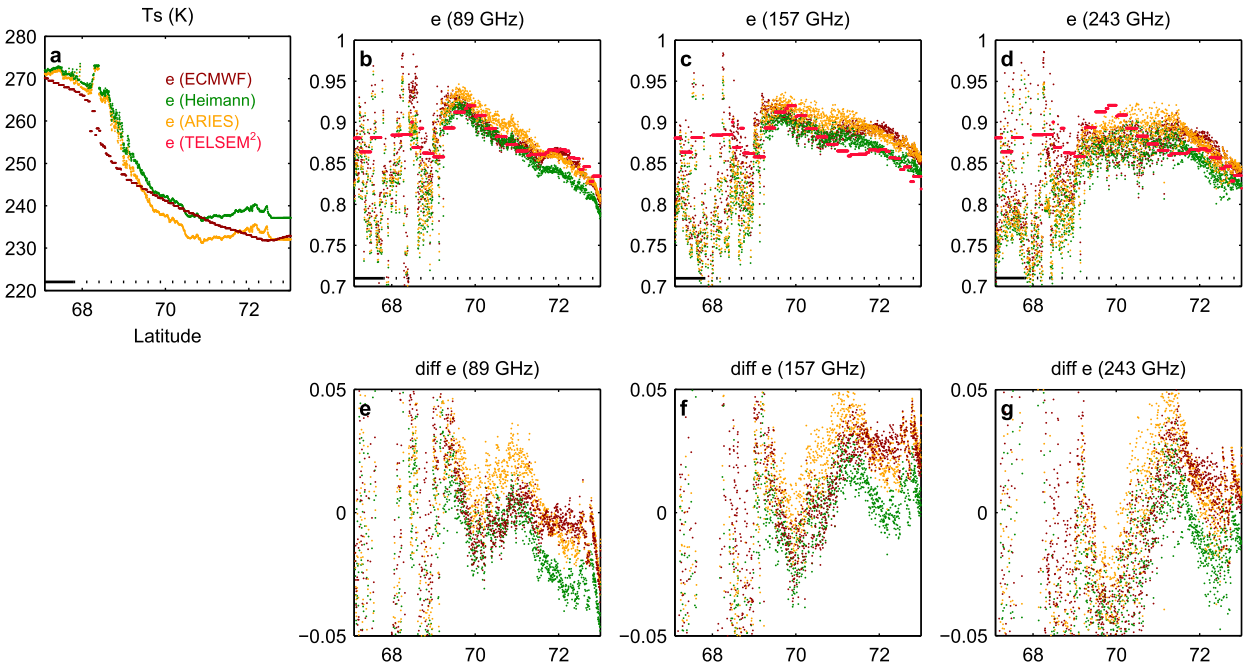

FIG. 14. (a) The surface temperature derived directly from the aircraft observations, along with the ECMWF-Interim database estimates for flight B896 on the way back from Greenland. (b)–(d) The corresponding emissivity at nadir from the aircraft measurements with the different T_s estimates, along with the corresponding TELSEM^2 emissivity. On the x axis, the solid black line indicates the presence of sea ice and the dotted line corresponds to the continent. (e)–(g) The differences between aircraft-retrieved emissivities and the TELSEM^2 emissivity [e(various airborne) − e(TELSEM^2)]. The brown dots represent e(ECMWF) − e(TELSEM^2), the green dots represent e(Heimann) − e(TELSEM^2), and the orange dots represent e(ARIES) − e(TELSEM^2).

For flight B896 at nadir (similar to Fig. 13), the emissivities have been estimated, using different T_s. The changes in T_s estimates have a significant impact on the emissivity retrieval, as expected, but none of the analyzed T_s estimates systematically improved the agreement with TELSEM^2. The emissivity aircraft retrievals in window frequencies are also presented for flight B898 (Figs. 15) at nadir and 40° on the way back from Greenland. The agreement with TELSEM^2 is very reasonable, and the spatial variability between 69° and 73°N is captured well. The histograms of the emissivity differences between the aircraft-derived estimates and TELSEM^2 results at nadir are shown in Fig. 16, over continental ice during the two flights, with the mean difference and its standard deviation for each frequency. At 89 GHz, the mean difference (−0.002) is much smaller than the mean difference between TELSEM and Météo-France and also between TELSEM and NOAA/MIRS [discussed in section 2b(4)]. As expected, the bias increases with atmospheric opacity, and it is larger near the water vapor lines at 183 (0.017) and 325 GHz (−0.022 GHz) than in the window channels at 89 (−0.002), 157 (0.012), 243 H (−0.011 H), and 243 V GHz (−0.013 V GHz). The mean difference and standard deviation are also calculated at 40° (not shown). The bias is very similar, and the standard deviation is slightly larger for each channel.

4. Conclusions

A parameterization of the snow and ice emissivities has been developed, for frequencies up to 700 GHz, in the framework of the preparation for the ICI on board the MetOp Second Generation (MetOp-SG). The objective is to provide realistic first-guess emissivity estimations for practical applications. Complex surface emissivity models might better capture small-scale spatial and temporal variability, but they require input information (e.g., snow depth, snow water equivalent, grain size, surface roughness) that are not available on a regular basis at global scale. Our parameterization relies upon satellite-derived emissivities up to 200 GHz, and it is anchored to the SSM/I TELSEM monthly climatology dataset (19–85 GHz). Météo-France and NOAA provided emissivities up to 190 GHz, calculated from SSMIS and AMSU-B observations. For continental snow and ice, the frequency dependence after 100 GHz is limited. For sea ice, the frequency dependence is more important and it is parameterized for some sea ice types. There is a general lack of information on the angular and

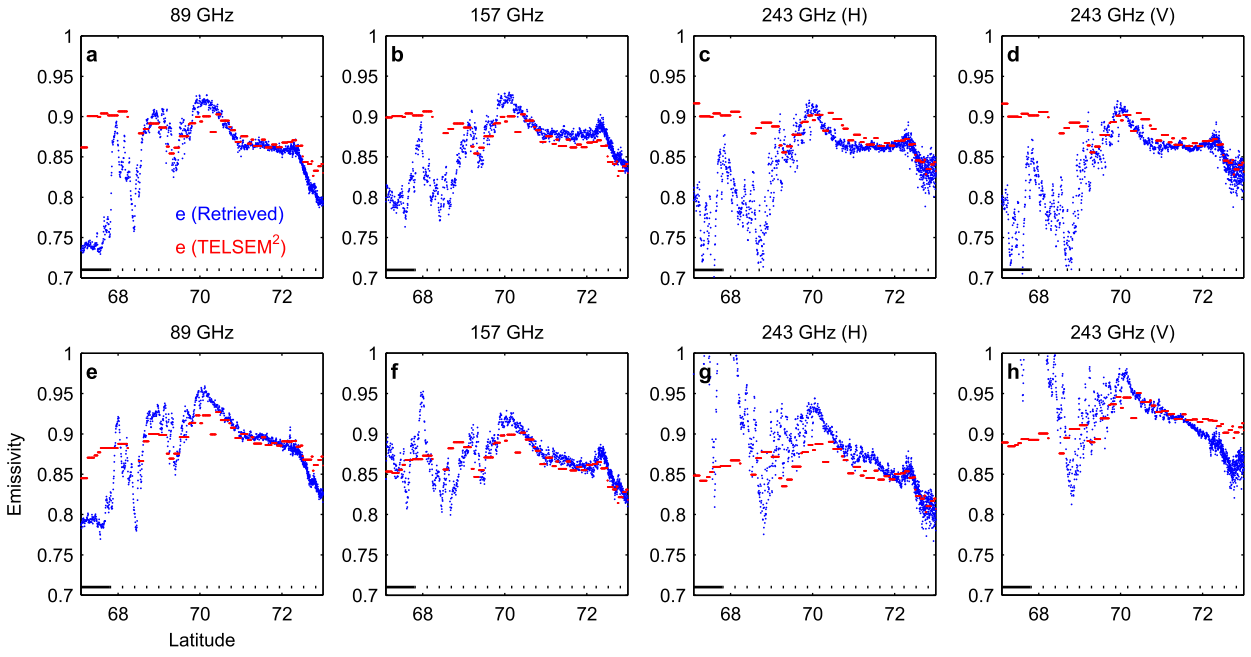

FIG. 15. The retrieved emissivity from MARSS and ISMAR observations for flight B898 as a function of latitude on the way back from Greenland at 89, 157, and 243 GHz (V and H): at (top) 0° and (bottom) 40° incidence angles. On the *x* axis, the solid black line indicates the presence of sea ice and the dotted line corresponds to the continent.

polarization dependence above 100 GHz. A conservative approach is adopted, following the polarization and angular dependencies obtained below 100 GHz, which may require revisions when more high-frequency data are available in the future. The TELSEM code has been updated to provide emissivity calculations up to 700 GHz (TELSEM^2) for all continents, including continental snow and ice and sea ice. TELSEM^2 is available to the community. The inputs of the code are the frequency, the incidence angle, the latitude, the longitude, and the month. It outputs the emissivity for both orthogonal polarizations, along with the error covariance matrix, with a 0.25° × 0.25° spatial resolution, at a monthly basis. TELSEM^2 will be included in the next version of the RTTOV package, a community radiative transfer code used by many numerical weather prediction centers, such as the Met Office, ECMWF, and Météo-France.

TELSEM^2 has been evaluated with observations between 89 and 325 GHz, on board the FAAM aircraft, during the COSMICS campaign over Greenland. The surface emissivities have been estimated from the aircraft observations, from the upwelling and downwelling radiances measured under dry conditions over Greenland, up to 325 GHz. At higher frequencies, the emissivity estimates were not reliable, due to the large atmospheric contribution to the TBs even at low level. Above continental snow and ice up to 325 GHz, TELSEM^2 is very consistent with the aircraft observations in spatially homogeneous regions. The frequency and angle dependences are well reproduced by the parameterization. The agreement at 89 and 157 GHz is even exceptional, considering that TELSEM^2 is assumed only to provide a realistic climatological first guess of the emissivities at a monthly scale. In coastal

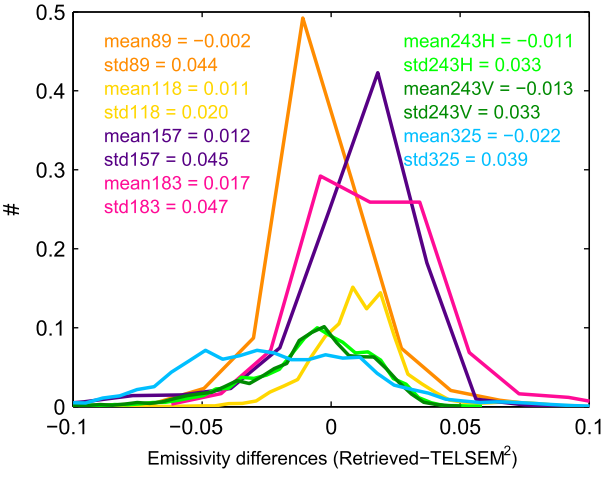

FIG. 16. Histograms of the emissivity differences between the aircraft-derived estimates and TELSEM^2 results, at nadir, over continental ice during flights B896 and B898. Each channel is represented by a different color, and the corresponding statistics (mean and std dev) are provided.

regions, the agreement can be affected by the differences in spatial resolution between the two estimates. Over sea ice, the aircraft estimates are highly variable both spatially and temporally, and comparisons with TELSEM^2 model were not conclusive. This is a first step toward the evaluation of the emissivity parameterization at millimeter and submillimeter frequencies over polar regions. More flights under a larger variety of surface and atmospheric conditions will have to be performed.

Acknowledgments. This study has partly been supported by a EUMETSAT contract ''Study on Surface Emissivity at Microwave and Sub-Millimeter Frequencies'' (EUM/CO/14/4600001473/CJA). We thank the crew and personnel involved in the COSMICS campaign. The BAe-146 research aircraft was operated by Directflight Ltd./Avalon and managed by the FAAM, which is jointly funded by the Met Office and Natural Environment Research Council (NERC). We thank Christophe Accadia, Vinia Mattioli, and Tim Hewison (EUMETSAT); Stephen English (ECMWF); Fuzhong Weng (NOAA); and James Hocking (Met Office) for discussions on these model developments. Die Wang is grateful to the CNES and AIRBUS (FR) for their financial support during her doctoral thesis. Some financial support for the data processing has also been provided by the CNES, through a TOSCA grant.

REFERENCES

Aires, F., C. Prigent, F. Bernardo, C. Jiménez, R. Saunders, and P. Brunel, 2011: A Tool to Estimate Land-Surface Emissivities at Microwave Frequencies (TELSEM) for use in numerical weather prediction. *Quart. J. Roy. Meteor. Soc.*, **137**, 690–699, doi:10.1002/qj.803.

Bernardo, F., F. Aires, and C. Prigent, 2013: Atmospheric water-vapour profiling from passive microwave sounders over ocean and land. Part II: Validation using existing instruments. *Quart. J. Roy. Meteor. Soc.*, **139**, 865–878, doi:10.1002/qj.1946.

Boukabara, S. A., and Coauthors, 2011: MiRS: An all-weather 1DVAR satellite data assimilation and retrieval system. *IEEE Trans. Geosci. Remote Sens.*, **49**, 3249–3272, doi:10.1109/TGRS.2011.2158438.

Cordisco, E., C. Prigent, and F. Aires, 2006: Snow characterization at a global scale with passive microwave satellite observations. *J. Geophys. Res.*, **111**, D19102, doi:10.1029/2005JD006773.

Eriksson, P., S. Buehler, C. Davis, C. Emde, and O. Lemke, 2011: ARTS, the atmospheric radiative transfer simulator, version 2. *J. Quant. Spectrosc. Radiat. Transfer*, **112**, 1551–1558, doi:10.1016/j.jqsrt.2011.03.001.

Fox, S., 2015: Microwave radiometer polarization description. Met Office Tech. Rep.

——, C. Lee, I. Rule, R. King, S. Rogers, C. Harlow, and A. Baran, 2014: ISMAR: A new submillimeter airborne radiometer. *MicroRad 2014: 13th Specialist Meeting on Microwave Radiometry and Remote Sensing of the Environment; Proceedings*, IEEE, 128–132, doi:10.1109/MicroRad.2014.6878923.

——, and Coauthors, 2016: ISMAR: An airborne submillimetre radiometer. *Atmos. Meas. Tech.*, **10**, 477–490, doi:10.5194/amt-2016-310,2016.

Harlow, R. C., 2009: Millimeter microwave emissivities and effective temperatures of snow-covered surfaces: Evidence for Lambertian surface scattering. *IEEE Trans. Geosci. Remote Sens.*, **47**, 1957–1970, doi:10.1109/TGRS.2008.2011893.

——, 2011: Sea ice emissivities and effective temperatures at MHS frequencies: An analysis of airborne microwave data measured during two Arctic campaigns. *IEEE Trans. Geosci. Remote Sens.*, **49**, 1223–1237, doi:10.1109/TGRS.2010.2051555.

——, and R. Essery, 2012: Tundra snow emissivities at MHS frequencies: MEMLS validation using airborne microwave data measured during CLPX-II. *IEEE Trans. Geosci. Remote Sens.*, **50**, 4262–4278, doi:10.1109/TGRS.2012.2193132.

Hewison, T. J., 2006: Aircraft validation of clear air absorption models at millimeter wavelengths (89–183 GHz). *J. Geophys. Res.*, **111**, D14303, doi:10.1029/2005JD006719.

——, and S. J. English, 1999: Airborne retrievals of snow and ice surface emissivity at millimeter wavelengths. *IEEE Trans. Geosci. Remote Sens.*, **37**, 1871–1879, doi:10.1109/36.774700.

——, N. Selbach, G. Heygster, J. P. Taylor, and A. J. McGrath, 2002: Airborne measurements of Arctic sea ice, glacier and snow emissivity at 24-183 GHz. *2002 IEEE International Geoscience and Remote Sensing Symposium: Remote Sensing; Integrating Our View of the Planet*, Vol. 5, IEEE, 2851–2855, doi:10.1109/IGARSS.2002.1026797.

Kalnay, E., and Coauthors, 1996: The NCEP/NCAR 40-Year Reanalysis Project. *Bull. Amer. Meteor. Soc.*, **77**, 437–471, doi:10.1175/1520-0477(1996)077<0437:TNYRP>2.0.CO;2.

Karbou, F., and C. Prigent, 2005: Calculation of microwave land surface emissivity from satellite observations: Validity of the specular approximation over snow-free surfaces? *IEEE Geosci. Remote Sens. Lett.*, **2**, 311–314, doi:10.1109/LGRS.2005.847932.

——, F. Aires, C. Prigent, and L. Eymard, 2005: Potential of Advanced Microwave Sounding Unit-A (AMSU-A) and AMSU-B measurements for atmospheric temperature and humidity profiling over land. *J. Geophys. Res.*, **110**, D07109, doi:10.1029/2004JD005318.

——, E. Gérard, and F. Rabier, 2006: Microwave land emissivity and skin temperature for AMSU-A and -B assimilation over land. *Quart. J. Roy. Meteor. Soc.*, **132**, 2333–2355, doi:10.1256/Qj.05.216.

——, F. Rabier, and C. Prigent, 2014: The assimilation of observations from the Advanced Microwave Sounding Unit over sea ice in the French global numerical weather prediction system. *Mon. Wea. Rev.*, **142**, 125–140, doi:10.1175/MWR-D-13-00025.1.

Mätzler, C., Ed., 2006: *Thermal Microwave Radiation: Applications for Remote Sensing.* IET Electromagnetic Waves Series, Vol. 52, Institution of Engineering and Technology, 584 pp.

Moncet, J.-L., P. Liang, J. F. Galantowicz, A. E. Lipton, G. Uymin, C. Prigent, and C. Grassotti, 2011: Land surface microwave emissivities derived from AMSR-E and MODIS measurements with advanced quality control. *J. Geophys. Res.*, **116**, D16104, doi:10.1029/2010JD015429.

Picard, G., L. Brucker, A. Roy, F. Dupont, M. Fily, A. Royer, and C. Harlow, 2013: Simulation of the microwave emission of multi-layered snowpacks using the Dense Media Radiative transfer theory: The DMRT-ML model. *Geosci. Model Dev.*, **6**, 1061–1078, doi:10.5194/gmd-6-1061-2013.

Prigent, C., W. B. Rossow, and E. Matthews, 1997: Microwave land surface emissivities estimated from SSM/I observations. *J. Geophys. Res.*, **102**, 21 867–21 890, doi:10.1029/97JD01360.

——, F. Chevallier, F. Karbou, P. Bauer, and G. Kelly, 2005: AMSU-A land surface emissivity estimation for numerical weather prediction assimilation schemes. *J. Appl. Meteor.*, **44**, 416–426, doi:10.1175/JAM2218.1.

——, F. Aires, and W. B. Rossow, 2006: Land surface microwave emissivities over the globe for a decade. *Bull. Amer. Meteor. Soc.*, **87**, 1573–1584, doi:10.1175/BAMS-87-11-1573.

——, E. Jaumouillé, F. Chevallier, and F. Aires, 2008: A parameterization of the microwave land surface emissivity between 19 and 100 GHz, anchored to satellite-derived estimates. *IEEE Trans. Geosci. Remote Sens.*, **46**, 344–352, doi:10.1109/TGRS.2007.908881.

——, P. Liang, Y. Tian, F. Aires, J.-L. Moncet, and S. A. Boukabara, 2015: Evaluation of modeled microwave land surface emissivities with satellite-based estimates. *J. Geophys. Res. Atmos.*, **120**, 2706–2718, doi:10.1002/2014JD021817.

Pulliainen, J. T., J. Grandeil, and M. T. Hallikainen, 1999: HUT snow emission model and its applicability to snow water equivalent retrieval. *IEEE Trans. Geosci. Remote Sens.*, **37**, 1378–1390, doi:10.1109/36.763302.

Rosenkranz, P. W., 1998: Water vapor microwave continuum absorption: A comparison of measurements and models. *Radio Sci.*, **33**, 919–928, doi:10.1029/98RS01182.

——, and D. H. Staelin, 1988: Polarized thermal microwave emission from oxygen in the mesosphere. *Radio Sci.*, **23**, 721–729, doi:10.1029/RS023i005p00721.

Rossow, W. B., and R. A. Schiffer, 1999: Advances in understanding clouds from ISCCP. *Bull. Amer. Meteor. Soc.*, **80**, 2261–2287, doi:10.1175/1520-0477(1999)080<2261:AIUCFI>2.0.CO;2.

Tonboe, R. T., 2010: The simulated sea ice thermal microwave emission at window and sounding frequencies. *Tellus*, **62A**, 333–344, doi:10.1111/j.1600-0870.2010.00434.x.

Tsang, L., J. Pan, D. Liang, Z. Li, D. W. Cline, and Y. Tan, 2007: Modeling active microwave remote sensing of snow using dense media radiative transfer (DMRT) theory with multiple-scattering effects. *IEEE Trans. Geosci. Remote Sens.*, **45**, 990–1004, doi:10.1109/TGRS.2006.888854.

Weng, F., B. Yan, and N. C. Grody, 2001: A microwave land emissivity model. *J. Geophys. Res.*, **106**, 20 115–20 123, doi:10.1029/2001JD900019.

Wiesmann, A., and C. Mätzler, 1999: Microwave emission model of layered snowpacks. *Remote Sens. Environ.*, **70**, 307–316, doi:10.1016/S0034-4257(99)00046-2.

Wilson, S. H. S., N. Atkinson, and J. A. Smith, 1999: The development of an airborne infrared interferometer for meteorological sounding studies. *J. Atmos. Oceanic Technol.*, **16**, 1912–1927, doi:10.1175/1520-0426(1999)016<1912:TDOAAI>2.0.CO;2.